

# Discussion on seismically triggered avalanches on Mars after the s1222a Marsquake

Antoine Lucas<sup>1</sup>, Ingrid J. Daubar<sup>2</sup>, Manon Le Teuff<sup>3</sup>, Clement Perrin<sup>4</sup>, Taichi Kawamura<sup>5</sup>, Liliya V Posiolova<sup>6</sup>, Philippe Lognonné<sup>7</sup>, Sebastien Rodriguez<sup>8</sup>, Domenico Giardini<sup>9</sup>, Grégory Sainton<sup>10</sup>, Anne Mangeney<sup>11</sup>, and Alfred McEwen<sup>12</sup>

<sup>1</sup>IPGP

<sup>2</sup>Department of Earth, Environmental, and Planetary Sciences, Brown University

<sup>3</sup>Université Paris Sciences et Lettres

<sup>4</sup>Laboratoire de Planétologie et Géodynamique

<sup>5</sup>Université Paris Cité, Institut de physique du globe de Paris, CNRS

<sup>6</sup>Malin Space Science Systems

<sup>7</sup>Université Paris Cité, Institute de physique de globe de Paris, CNRS

<sup>8</sup>Institut de Physique du Globe de Paris (IPGP), Université Paris-Diderot

<sup>9</sup>ETH Zürich

<sup>10</sup>Université paris Cité, Institut de physique du globe de Paris, CNRS

<sup>11</sup>Institut de Physique du Globe de Paris

<sup>12</sup>University of Arizona

November 14, 2023

# Possibly seismically triggered avalanches after the S1222a Marsquake and S1000a impact event

Lucas A.<sup>1</sup>, Daubar I. J.<sup>2</sup>, Le Teuff M.<sup>1</sup>, Perrin C.<sup>3</sup>, Kawamura T.<sup>1</sup>, Posiolova L.<sup>4</sup>, Lognonné P.<sup>1</sup>, Rodriguez S.<sup>1</sup>, Giardini D.<sup>5</sup>, Sainton G.<sup>1</sup>, Mangeney A.<sup>1</sup>, McEwen A.<sup>6</sup>

<sup>1</sup>Université Paris Cité, Institut de physique du globe de Paris, CNRS, F-75005, Paris, France

<sup>2</sup>Brown University, Providence, RI, USA

<sup>3</sup>Nantes Université, Université d'Angers, Le Mans Université, CNRS, UMR 6112, Laboratoire de Planétologie et

Géosciences, UAR 3281, Observatoire des Sciences de l'Univers de Nantes Atlantique, Nantes, France

<sup>4</sup>Malin Space Science System, San Diego, CA, USA

<sup>5</sup>ETH, Zurich, Switzerland

<sup>6</sup>U. Arizona, USA

## Key Points:

- On May 4, 2022, a major martian seismic event was recorded
- We catalog seismically induced dust avalanches in the area of the estimated epicenter
- We discuss avalanche triggering conditions and derive a possible epicenter location based on avalanche spatial density

---

Corresponding author: A. Lucas, [lucas@ipgp.fr](mailto:lucas@ipgp.fr)

## Abstract

Ground motion from seismic events detected by the SEIS/InSight seismometer on Mars could potentially trigger dust avalanches. Our research demonstrates that the seismic event S1000a caused a significant number of dust avalanches. In contrast, following the seismic event S1222a, there was only a modest increase in avalanche occurrences. Orbital observations of the area surrounding the projected location of the S1222a quake reveal notable topographic features, such as North-South ridges and impact craters. We utilize orbital imagery to evaluate the rate of avalanches and explore how the S1222a event might have influenced this rate. The S1222a event appears to be a plausible factor contributing to the observed increase in avalanches. Our further analysis of the epicenter location aims to clarify how it aligns with the avalanches' spatial distribution, offering insights into the regional topography.

## Plain Language Summary

We explore the potential effects of seismic aftermath on Mars, focusing on how large seismic events might trigger dust avalanches and mass wasting. Our analysis of orbital data reveals that the affected area is characterized by steep slopes, predominantly around crater walls, where dust accumulation is substantial. This geological setup makes the region particularly prone to dust avalanches. Large seismic events are known to cause ground acceleration, which can reduce material cohesion and friction, or increase tangential strain. These changes are conducive to mass wasting. Based on our research, we propose that the S1222a marsquake could be a primary factor contributing to the observed increase in avalanche activity, as evidenced by our analysis of orbital imagery. This finding sheds light on the dynamic interplay between seismic activity and surface processes on Mars.

## 1 Introduction

On May 4, 2022, a major seismic event (Kawamura et al., 2023) was recorded by the SEIS instrument (Lognonné et al., 2019) of the InSight mission (Banerdt et al., 2020). It was an unprecedented marsquake in the SEIS recording period with an estimated moment magnitude of  $M_W^{Ma}$  4.7 (InSight Marsquake Service, 2022). In comparison, 95% of events recorded by SEIS since landing in November 2018 have a magnitude below 3.5 (Clinton et al., 2021; Böse et al., 2021; Ceylan et al., 2022; Knapmeyer et al., 2023). As for some of the InSight events, a location was estimated with a back-Azimuth (bearing from the event toward InSight) of  $101^\circ$  ( $96^\circ$ - $112^\circ$ ) and an epicentral distance  $\Delta = 37^\circ$  ( $\pm 1.6^\circ$ ) which places the event epicenter at the location of  $3.0^\circ\text{S}, 171.9^\circ\text{E}$  (Kawamura et al., 2023) (green star on Fig. 1). Other nearby locations for the epicenter have also been proposed (Panning et al., 2023; Kim et al., 2022) (Fig. 1). No new impact crater has been reported that could be the source of this event (Fernando et al., 2023). The region shows many topographic features including a few tectonic structures expressed as north-south wrinkle ridges (Knapmeyer et al., 2006) and impact craters (Fig. 1). To the east of this region, the only major structures are Appollinaris Patera, a Noachian volcano (Tanaka et al., 2014) about 200 km in diameter, and a large alluvial fan spanning southwards from the volcano's rim.

From orbital images, dust avalanches (also known as slope streaks) have been identified in this region (orange symbols on Fig. 1). These are known active mass wasting processes occurring on Mars in several contexts (Ferguson & Lucchitta, 1984; Sullivan et al., 2001; Aharonson et al., 2003; Schorghofer et al., 2002, 2007; Schorghofer & King, 2011; Gerstell et al., 2004; Baratoux et al., 2006; Chuang et al., 2007; Bergonio et al., 2013; Heyer et al., 2019, 2020; Valantinas et al., 2021). They appear as relatively dark or bright streaks on steep dust-covered slopes and occur in regions with a high albedo and low to very low thermal inertia (Sullivan et al., 2001; Aharonson et al., 2003). Dust avalanches

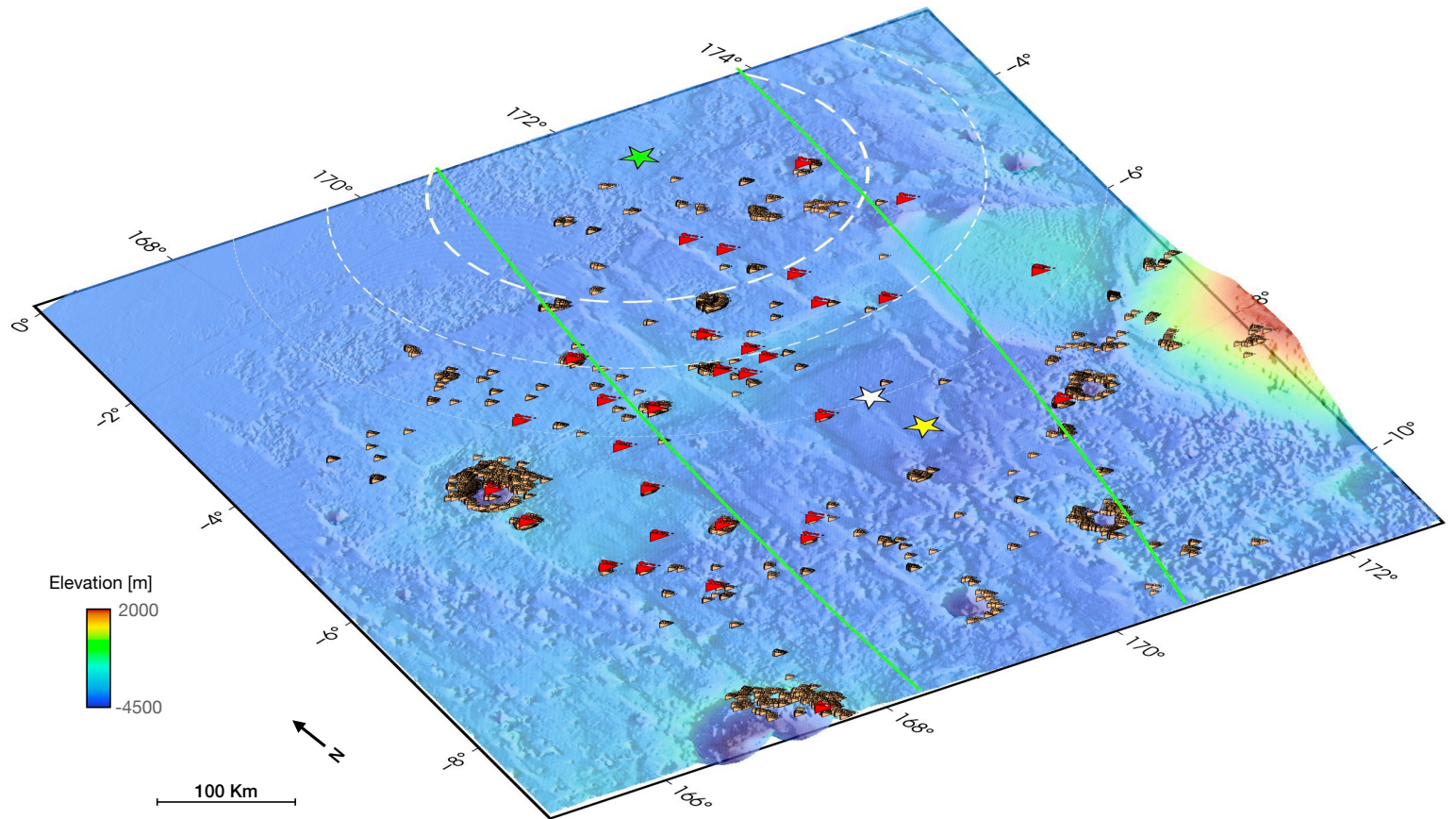


**Figure 1.** Regional map of dust avalanches near the S1222a event estimated location (green star with associated green ellipse, (Kawamura et al., 2023)). The white star is the location estimated by multi-orbit surface waves Panning et al. (2023). The yellow star shows the estimated location according to surface waves (Kim et al., 2022). Dashed white circles represent epicentral distances  $\Delta = 2^\circ, 3^\circ$  and  $4^\circ$  from the green star. Orange symbols are all avalanches mapped. Red symbols show where avalanches are observed on post-event images. Basemap is the MOLA elevation map (Smith et al., 2001).

68 on Mars typically appear darker than the surrounding terrain. This is likely due to the re-  
 69 moval of lighter-colored surface dust by the avalanches. When a slope streak is formed,  
 70 loose dust and sand on the surface are mobilized and cascade down the slope, exposing  
 71 the darker, underlying material (Malin et al., 2007; Dundas, 2020). This material may be  
 72 darker due to several factors, such as the presence of iron-rich minerals or alteration by  
 73 weathering processes (Christensen et al., 2001). In addition, the removal of surface dust  
 74 by the avalanches may expose a rougher, more textured surface, which can scatter and ab-  
 75 sorb more light, making the streak appear even darker. Many studies discuss possible trig-  
 76 gering conditions and emplacement mechanisms. Purely dry avalanches of fine dust have  
 77 been explored from the perspective of both observations (Schorghofer et al., 2007; Phillips  
 78 et al., 2007; Dundas, 2020), and numerical simulations (Lucas, 2010). Spring discharge  
 79 involving salty groundwater and/or brines in the shallow subsurface has been proposed  
 80 (Ferris et al., 2002; Miyamoto, 2004; Head et al., 2007; Kreslavsky & Head, 2009; Bhard-  
 81 waj et al., 2017, 2019). Other possible triggers include wind (Baratoux et al., 2006; Heyer  
 82 et al., 2019) or seismic activity from impacts or internal forces (Chuang et al., 2007) have  
 83 been proposed.

84 While previous studies looked at boulder falls and associated tracks triggered by  
 85 possible paleo-seismic activity (Roberts et al., 2012; Brown & Roberts, 2019), no previ-  
 86 ous work could have directly tested the possibility of seismically induced mass wasting on  
 87 Mars due to a lack of seismic event records before the InSight mission. In the framework  
 88 of the recent seismic events S1000a and S1222a, we investigate the effects of the induced  
 89 ground acceleration aftermaths as a potential triggering mechanism for dust avalanches  
 90 in the vicinity of the located epicenter. To do so, we conduct regional mapping of the  
 91 avalanches from pre-event and post-event imagery in order to estimate the effect of the  
 92 marsquake and impact crater on the rate of avalanches. We take into account possible bi-  
 93 ases due to the limited number of images, the time span between images, the sub-surface  
 94 properties through thermal behavior, and the various sensitivities of each camera sensor.

## 95 2 Methods

### 96 2.1 Orbital data and mapping

97 As soon as the S1222a event was detected by SEIS and an estimate of the epicenter  
 98 location was provided, we investigated orbital observations provided by the Context (CTX)  
 99 and High Resolution Imaging Science Experiment (HiRISE) cameras (Malin et al., 2007;  
 100 McEwen et al., 2007), both on board the Mars Reconnaissance Orbiter (MRO). Along  
 101 with MRO imagery, we examine images from the Mars Global Surveyor (MGS)/Mars  
 102 Orbiter Camera (MOC) and THEMIS-Vis/Odyssey (Fergason et al., 2006). This led to a  
 103 set of hundreds of images acquired before the seismic event. In addition, we requested  
 104 new MRO observation over areas where we mapped avalanches inside the uncertainty area  
 105 (Kawamura et al., 2023) (Fig. 1, Supp. Info text S1). At the time of writing this paper, a  
 106 dozen HiRISE images and thirty new CTX observations were obtained, all acquired after  
 107 the S1222a seismic event. In addition to imagery, we used Digital Terrain Models (DTMs)  
 108 from both Mars Orbiter Laser Altimeter (MOLA, Smith et al. (2001)) and High Reso-  
 109 lution Stereo Camera (HRSC, Neukum and Jaumann (2004)), the geological map from  
 110 Tanaka et al. (2014) and the thermal inertia map (Christensen et al., 2004) (See Supp.  
 111 Info text S2), which all provide contextual information. All the data have been combined  
 112 into a Geographical Information System (GIS) in order to manually map all avalanches  
 113 in the region of interest (Fig. 1), by two independent people (see Supp Info S1 for details  
 114 on the imagery processing and mapping). The older observations, provided by both MOC  
 115 and THEMIS-Vis, were only used for confirming the very low fading rate (Sullivan et al.,  
 116 2001), being in good agreement with the dust activity reported in this region (Battalio &  
 117 Wang, 2021).

### 118 2.2 Estimates of avalanche rate and statistics

119 Avalanche rate  $q$  is obtained from equation provided in Aharonson et al. (2003):

$$q = 100 \times \frac{\Delta n}{n\Delta t}, \quad (1)$$

120 where  $n$  is the total number of avalanches observed in both the two overlapping im-  
 121 ages,  $\Delta n$  being the newly observed avalanches on the recent image and not in the older  
 122 image, and  $\Delta t$  being the time span between the two observations in Martian years. This  
 123 rate  $q$  is expressed in % of new events/Martian year (Aharonson et al., 2003). This method  
 124 has also been used by recent work (Heyer et al., 2019). The time periods between overlap-  
 125 ping images in our database range from  $\sim 0.3$  to almost 7 martian years.

126 Finally we agglomerate avalanches in the same location (i.e. crater) and hence to  
 127 compute the avalanche rate in each area where new events can be observed between two  
 128 overlapping images. As opposed to a squared binning, hexagons are more similar to cir-  
 129 cles, hence they better translate data aggregation around the bin center. As most areas

covered by avalanches in this region are impact craters, this provides a more valuable way to decipher the avalanche coverage.

### 3 Results and discussion

#### 3.1 Evidence of avalanches triggered after S1000a impact event

Before discussing S1222a event, we investigated S1000a impact event which occurred on September 18 2021, and left a crater over 150 m in diameter at  $38.1^\circ\text{N}; -79.87^\circ\text{E}$  (Fig. 2). This event was recorded by SEIS and then orbital imagery revealed its actual location. Its magnitude was estimated to be around  $M_w^{Ma}$  4.1, hence about 25 times smaller than S1222a in energy (Ceylan et al., 2022; Posiolova et al., 2022). By analysing all pre-event images including CTX, and HRSC and post-event HiRISE images, we could map a very large number of avalanches not seen in pre-event imagery. By looking back in time using all available images, including MOC/MGS, we observed that these areas were not covered by dust avalanches prior to the impact event (Fig. 2).

We looked at the the density distribution of the new avalanches (as seen on the post-event images and having the same radiometric signature, hence the same age) as a function of their respective distance to the impact crater (histogram inset in Fig. 2). This distribution follows a bell-shaped curve. As seen on Earth, seismically triggered mass-wasting is absent very close to the epicenter, and increases at farther distances until it decreases again at the farthest distances (e.g., Tatar, 2010; Livio & Ferrario, 2020). Nonetheless, the mechanism here is different. It is very likely that the avalanches are triggered by secondary impacts, and not seismic waves. As an example of a typical scenario, ejecta leaving the primary impact at a velocity  $v = 200 \text{ m}\cdot\text{s}^{-1}$ , with a launch angle of  $\theta = 45^\circ$ , will have a ballistic flight time  $t_f$  of 76 sec (i.e.,  $t_f = 2 \times v \sin \theta / g$ ), and will land at a distance  $d_l = 10.78 \text{ km}$  (neglecting the air friction,  $d_l = v \cos \theta \times t_f$ ). Hence, the histogram in the inset of figure 2 is similar to the statistical distribution of secondary ejecta impacting the ground. This correlation indicates those secondary impacts are a likely source for the avalanches. Of course, the S1000a event is an ideal case. First of all, we know the position of the epicenter perfectly well, thanks to the orbital imagery revealing the source crater. What's more, the presence of northeast-southwest trending ripples implies the presence of uniformly distributed topographic slopes as moving away from the impact crater, hence the avalanche susceptibility. Note that Burleigh et al. (2012) demonstrated that impact blast can trigger slope streaks. The S1000a event also shows that an impact with a seismic magnitude  $M_w^{Ma}$  4.1 can trigger a very large number of avalanches on Mars. As such, this is likely to be discussed more thoroughly in a following work which would evaluate the ballistic recomposition in order to evaluate potential effects of secondary impacts on the dust avalanche triggering. However, the ground accelerations caused by a surface impact and a deep earthquake are not the same. So, in view of our results for the S1000a event, we discuss our results for S1222a in the following sections.

#### 3.2 Evidence of avalanche rate increase in post-marsquake S1222a images

We analyzed all image pairs over the whole area of interest near the S1222a estimated epicenter. We identified 4532 avalanches (orange symbols in Figure 1). More than 200 avalanches were identified on pre-event images (over the 2005–2021 period), and 122 were identified on the post-event CTX images with respect to their 2005–2021 period counterparts respectively. An example is given in Figure 3-a. Note that, while spurious avalanches may have been detected (e.g., yellow symbols in Fig. 3-a), we only took into account the robust observations of new avalanches (e.g., red symbols in Fig. 3-a). For the statistical robustness, we then derived avalanche rates  $q$  for each CTX/CTX pair only. When times series were available, we derived avalanche rate chronicles (Fig. 3-b). As exemplified on Fig. 3-b, a strong increase of  $q$  is observed after the S1222a event. Indeed, over the whole area of interest (Fig. 1), the pre-event rates (circles in fig. 3-c) lie around

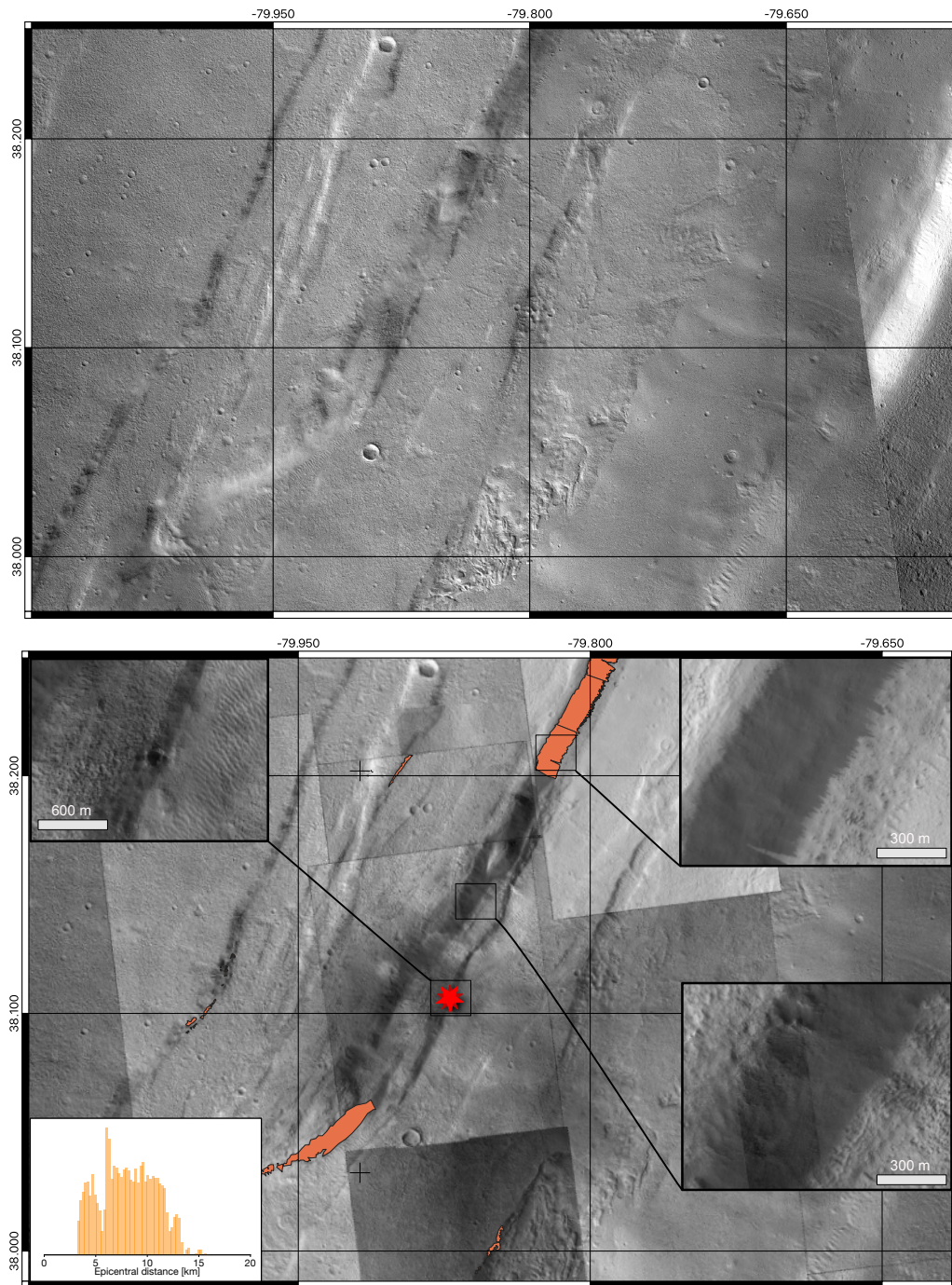


**Figure 2.** (top) Pre-event CTX mosaic around the impact location of S1000a (dated from 2018-09-12) showing absence of any dust avalanches. (bottom) Post-event HiRISE mosaic on top of CTX images around the impact location of S1000a event (red star) with associated triggered avalanches (orange areas). Insets show close-up on the crater, the avalanches areas and slopes without new avalanches (from top-left, to bottom-right, respectively). The density distribution of avalanches with respect to the epicentral distance is shown in the bottom-left inset.

180 2.6%.MYear<sup>-1</sup> with a maximum value of 6%.MYear<sup>-1</sup>, accounting for uncertainties fol-  
 181 lowing Aharonson et al. (2003). These values are in agreement with in previous work  
 182 (Aharonson et al., 2003), and avalanche rates do not differ substantially across the region  
 183 covered by our study. In contrast, post-event values of  $q$  show a significantly different dis-  
 184 tribution both spatially and in amplitude (Figure 3-c,d). While most rates still fall below  
 185 10%, we observe that in 9 places, the rates are >10%, as high as 40% (excluding outlier,  
 186 Figure 3-d). If we keep only the sub-10% values, the average is the same as that before  
 187 the seismic event (2.6%/MYear), and there is also no dependence on the epicentral dis-  
 188 tance. Interestingly, the highest post-event  $q$  (>20%) are found at the smallest distances  
 189 from the epicenter of the S1222a event proposed by Kawamura et al. (2023). When relat-  
 190 ing the derived avalanche rate  $q$  to the epicentral distance  $\Delta$  with respect to the estimated  
 191 location from Kawamura et al. (2023), we obtained a slight decreasing trend of  $q$  with  $\Delta$ .  
 192 Finally we also verified that temporal sampling of the orbital images ( $\Delta t$ ) does not bias the  
 193 avalanche rate estimates (Fig. 3-e).

194 To address the limited number of observations, we employed a permutation test, also  
 195 known as bootstrapping (Efron & Tibshirani, 1993; Davison & Hinkley, 1997). This non-  
 196 parametric approach does not rely on specific distribution assumptions about the data. We  
 197 began by calculating the avalanche rate for each CTX/CTX pair for both pre-event and  
 198 post-event observations, determining the mean difference as our observed statistic. Then,  
 199 we merged the pre-event and post-event rates, treating them as a combined dataset with-  
 200 out distinction of their original times. This pooled data was randomly shuffled to create  
 201 new groups, preserving the original group sizes. We calculated the permuted test statis-  
 202 tic by assessing the avalanche rate in this permuted data. This permutation process was  
 203 iterated a million times, generating a distribution of test statistics under the hypothesis of  
 204 no marsquake influence. Comparing our observed statistic to the 95% confidence inter-  
 205 val derived from bootstrapping, we found that the post-event avalanche rates in all CTX  
 206 observations exceeded 95% of the bootstrap statistic distribution. This indicates a signifi-  
 207 cant increase in avalanche activity following the seismic event. However, it is important to  
 208 note that the area studied includes locations possibly too distant from the epicenter to be  
 209 affected by the marsquake. Focusing on rates exceeding 6%.MYear<sup>-1</sup>, the post-marsquake  
 210 rates surpassed the 99.98% confidence level. These findings, along with the detailed boot-  
 211 strapping procedure, are outlined in Algorithm 1 and illustrated in Figure 4.

---

**Algorithm 1:** Assessing Influence of marsquake on avalanche rate

---

**Input:** Pre-event image pairs ( $n, \Delta n, \Delta t$ )

**Input:** Post-event image pairs ( $n, \Delta n, \Delta t$ )

Define the observed test statistic:  $\Delta n_{obs}$  (change in the number of avalanches),  $n_{obs}$  (number of avalanches), and  $\Delta t_{obs}$  (time difference between images);

Combine the before and after data into a single pool, disregarding their original labels;

Perform resampling with replacement: Randomly sample, with replacement, from the pooled data to create a bootstrap sample of the same size as the original data set. Repeat this process to generate a large number of bootstrap samples.

Calculate the test statistic for each bootstrap sample: Compute the rate of avalanches for each bootstrap sample, given by  $\frac{\Delta n_{boot}}{n_{boot} \Delta t_{boot}}$  ;

Calculate the bootstrap statistic distribution: Collect the calculated test statistics from step 4 to form the bootstrap distribution of the test statistic;

Calculate the confidence interval: Determine the desired confidence level (e.g., 95%).

Compute the lower and upper percentiles of the bootstrap distribution corresponding to the chosen confidence level;

**Output:** Assessment of marsquake influence

---

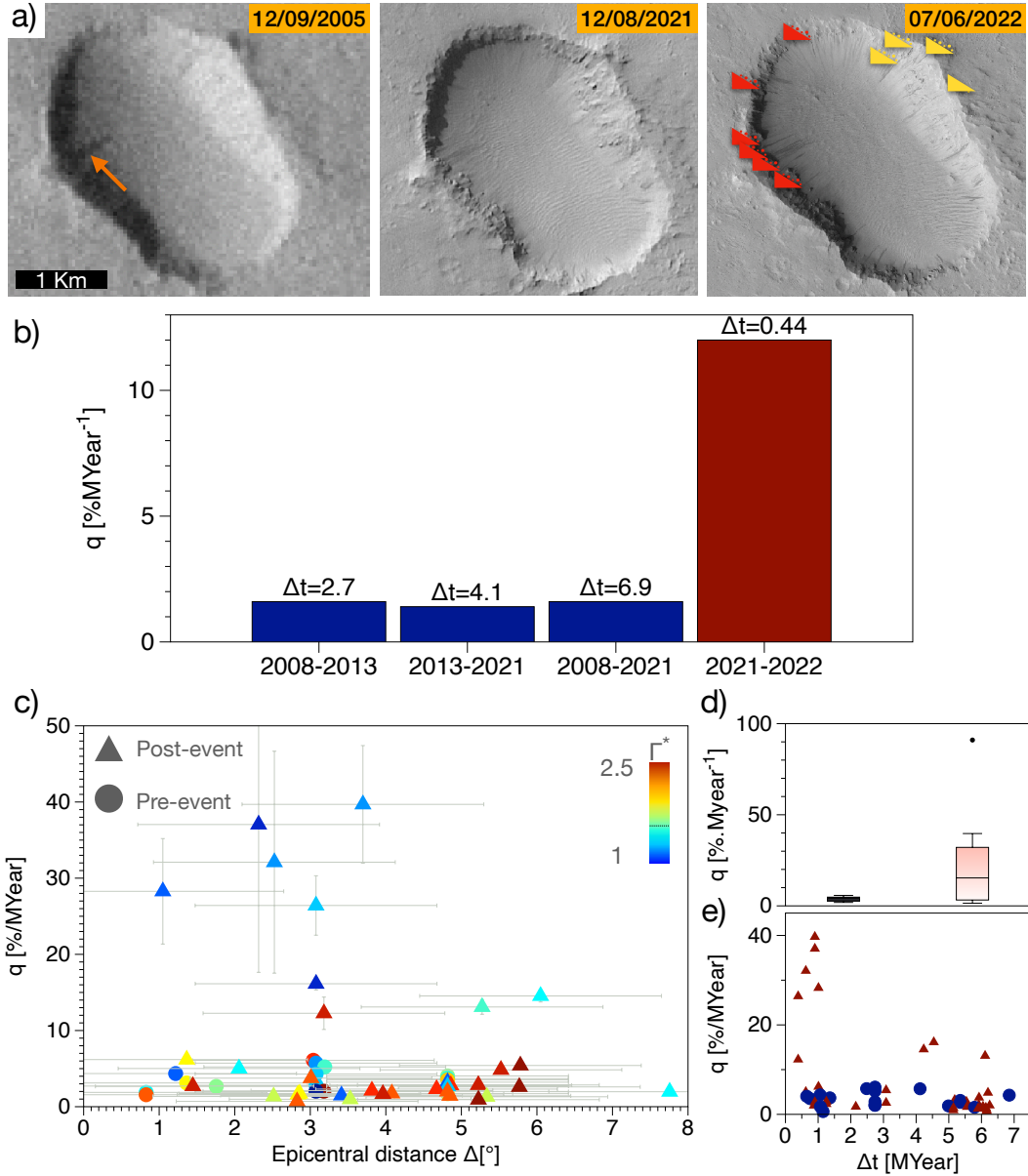


**Figure 3.** a) Image times series with THEMIS-Vis image V1768100 (17m/pixel) taken in 2005, CTX image N21\_070520\_1744\_XI\_05S189W (6m/pixel) taken 8 months before S1222a, and an HiRISE image (down-sampled to 5m/pixel) ESP\_074357\_1745 taken a few weeks after the marsquake. New avalanches marked with the red symbols. Additional spurious avalanches are indicated with the yellow symbols, b) time series of avalanche rate  $q$  over the 2008-2022 period. c) Avalanche rate  $q$  as a function of the epicentral distance  $\Delta$  (with respect to the green star of Fig. 1) for CTX/CTX image pairs. Symbols are associated to pre-event (circles) or post-event (triangles). Color scales with the ratio of apparent thermal inertia ( $\Gamma^*$ , with dashed line at 1.5). d) Box plot of avalanche rates for pre-event pairs (black) and pre/post-event pairs (red). e) Avalanche rate  $q$  as a function of timespan  $\Delta t$ . Note that some symbols can overlap each other on both plots.

212

### 3.3 Discussion on the relative thermal inertia and the triggered avalanches

213

Subsurface properties at shallow depths can be analyzed through thermal inertia, which indicates how solar energy absorption and subsequent subsurface heat propagation

214

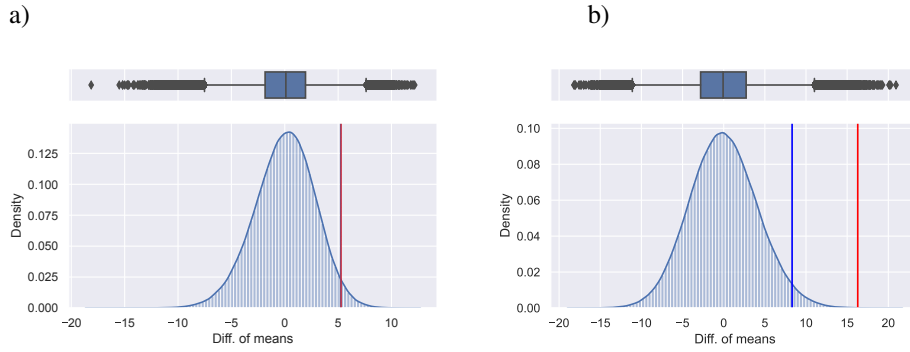


**Figure 4.** Bootstrapping statistics. (a) accounting for the whole data set, (b) when only considering  $q>5$  for the post-event observation. (top-panel) Quantiles of the permutation tests. (bottom-panel) The distribution of the permutation tests. The thin vertical blue lines gives the 95% of the test statistics distribution. The dashed red vertical line shows the observed statistics.

215 relate to material properties. Thermal inertia is represented as  $\Gamma \equiv \sqrt{\kappa_e(1-p)\rho C(T)}$ ,  
 216 where  $\kappa_e$  denotes effective thermal conductivity,  $p$  is porosity,  $\rho$  represents density, and  
 217  $C(T)$  is the specific heat capacity. Therefore, low thermal inertia can indicate high poros-  
 218 ity, low density, small grain size, or a combination of these factors. As Sullivan et al.  
 219 (2001); Aharonson et al. (2003) previously demonstrated, dust avalanches on Mars typi-  
 220 cally occur on steep slopes and are exclusively found in areas with low thermal inertia.

221 It's important to note that thermal inertia values are derived from models and as-  
 222 sumptions, as detailed by Christensen et al. (2004). Due to significant variations between  
 223 orbits, we calculate the ratio of the apparent value of thermal inertia at avalanche scar  
 224 location with respect to the median value on the surrounding plains, and named it  $\Gamma^* =$   
 225  $\Gamma_{avalanche}/\Gamma_{plain}$ . The methodology for extracting this ratio of apparent value is ex-  
 226 plained in our supplementary information (see Supp. Info text S2). Interestingly, avalanches,  
 227 which form on steep slopes, are associated with higher ratio of apparent thermal inertia  
 228 than the surrounding terrain, likely due to a thicker dust mantle in the latter. By exam-  
 229 ining the ratio of apparent thermal inertia over pixels at avalanche scarps, we found that  
 230 areas with the lowest  $\Gamma^*$  values experience the most significant increases in avalanche rates  
 231 (see Fig. 3-c). Specifically, when  $\Gamma^* \gg 1.5$ , post-event avalanche rates do not exceed  
 232 pre-event rates. Conversely, an increase in  $q$  is observed when  $\Gamma^* < 1.5$ . This leads us to  
 233 conclude that post-event avalanche susceptibility on Mars is primarily influenced by scarp  
 234 locations with steep slopes and low apparent thermal inertia. Such conditions correspond  
 235 to the most unconsolidated terrains or areas with fine granular material.

### 236 3.4 Discussion on the epicentral distance and possible sources of the quake

237 Although the epicentral distance is far from being the only parameter that controls  
 238 the avalanche rates, it remains an important control factor. The reason is that the transition  
 239 between a static state and a flowing state is modelled by introducing a threshold allow-  
 240 ing the material to flow. This has been shown to quantitatively capture debris and rock  
 241 avalanche morphodynamics on Mars (Lucas, 2010; Lucas & Mangeney, 2007; Lucas et  
 242 al., 2011, 2014) (see Supp. Info Text. S3). Nonetheless, local geology, fractures, after-  
 243 shocks and historical events will have a significant effect on the aftermaths of an earth-  
 244 quake by leading the slopes close to failure (Tatard, 2010; Livio & Ferrario, 2020; Chen  
 245 et al., 2020; Rosser et al., 2021; Lombardo & Tanyas, 2022). Taking into account all these  
 246 considerations, the rate would not be expected to be controlled only by epicentral distance.  
 247 However, our constraints on the characteristics of the marsquake are weak, especially in

248 terms of depth, focal mechanisms, and therefore the resulting ground acceleration. Our  
 249 knowledge on the geological heterogeneity is also poorly constrained. Also, compared to  
 250 terrestrial standards, this marsquake remains a small event. Nonetheless, small seismic  
 251 events have shown to significantly increase the rate of landslides on Earth (Martino et al.,  
 252 2022). Indeed, recent studies show that even very small amplitude seismicity may trigger  
 253 instabilities on metastable slopes (Bontemps et al., 2020; Durand et al., Minor revision).

254 Nonetheless, under the hypothesis that event S1222a did trigger avalanches, we con-  
 255 sidered the empirical model proposed by Livio and Ferrario (2020) which relates the dis-  
 256 tribution of triggered avalanches  $N_{ava}$  with the epicentral distance  $\Delta$ :

$$G(\mathbf{m}) = N_{ava} = a \exp \left[ - \left( \frac{\Delta - b}{c} \right)^2 \right], \quad (2)$$

257 where  $a$  is the amplitude of the distribution,  $b$  the distance of the peak amplitude and  $c$   
 258 the width of the distribution. While we do not have images just before and just after the  
 259 event, we derived an estimation of the number of triggered avalanches from this relation-  
 260 ship:

$$N_{ava} = \Delta n - \bar{q} \times n \Delta t / 100, \quad (3)$$

261 where  $\bar{q}$  is the long-term avalanche rate (i.e., we conservatively considered  $6\% \text{MYear}^{-1}$ ).  
 262 Because the avalanche susceptibility is not evenly distributed (i.e., steep slopes only lo-  
 263 cated inside impact craters, non-homogeneous surface/sub-surface properties), we only  
 264 consider observations that meet the following criteria:  $\Gamma^* < 1.93$ , and  $\Delta t < 1.5 \text{MYear}$ ,  
 265 to only account for the lowest thermal inertia (see Fig. 3) and the smallest time span be-  
 266 tween images to reduce biases. Then, we used a Monte Carlo method to invert the most  
 267 probable epicenter location using a maximum likelihood function with a Laplacian distri-  
 268 bution of errors (Mosegaard & Tarantola, 1995) (See Supp Info Text S4). The resulting  
 269 probability distribution of the epicenter under all of these considerations is given in Fig-  
 270 ure 5. It is situated in between the locations obtained from both body and surface waves  
 271 analysis respectively (Kawamura et al., 2023; Panning et al., 2023; Kim et al., 2022), then  
 272 included in the uncertainty ellipses of epicentral locations (green contours in Fig. 5).

273 This distribution can lead us to two different interpretations regarding the source  
 274 mechanism of the quake, mainly related to internal tectonic activity. A first hypothesis  
 275 would be based on the fact that our distribution is slightly shifted toward the East from  
 276 the wrinkle ridges, on the flanks of Apollinaris Patera. It is now well supported that Mars  
 277 still hosts remnant volcano-tectonic activity, especially along Cerberus Fossae (Giardini et  
 278 al., 2020; Horvath et al., 2021; Perrin et al., 2022; Stähler et al., 2022), possibly due to  
 279 the presence of a plume (Broquet & Andrews-Hanna, 2022), and associated with normal  
 280 slip motion (Brinkman et al., 2021; Jacob et al., 2022). While the moment tensor analy-  
 281 sis of the S1222a event can give very different slip motions, NNW-SSE normal faulting is  
 282 a possible solution (Maguire et al., 2023), highlighting a possible activity of Apollinaris  
 283 Patera at depth. However, unlike Cerberus Fossae, Apollinaris Patera is an old Noachian  
 284 volcano, thus it seems unlikely that remnant volcanic activity would be present at shallow  
 285 depth. A second hypothesis would be related to the 450 km long wrinkle ridge, trending  
 286 NNE-SSW, and cross-cutting the Hesperian terrains between the two epicentral locations  
 287 (black lines in figure 5). The probability distribution of the epicenter inferred from the  
 288 avalanche rate is about 30 to 60 km East of this major structure. The shape of the topo-  
 289 graphic profile across the ridge is an asymmetric arch-ridge, with a steep slope facing  
 290 West and a shallow slope facing East (Fig. 1), which would imply a main East-dipping  
 291 thrust at depth (Andrews-Hanna, 2020). Assuming a fault dip of  $34^\circ$  to  $42^\circ$  for arch-ridges  
 292 (Andrews-Hanna, 2020), a probability distribution situated about 30 to 60 km East of the  
 293 wrinkle ridge would lead to a hypocentral depth ranging from 20 to 54 km. This range  
 294 of depth is in agreement with the best solutions found by Maguire et al., 2023. They also  
 295 present mainly reverse slip motions striking E-W to NW-SE, which is not optimally orien-  
 296 ted with the overall wrinkle ridge observed from orbital imagery. However, local large

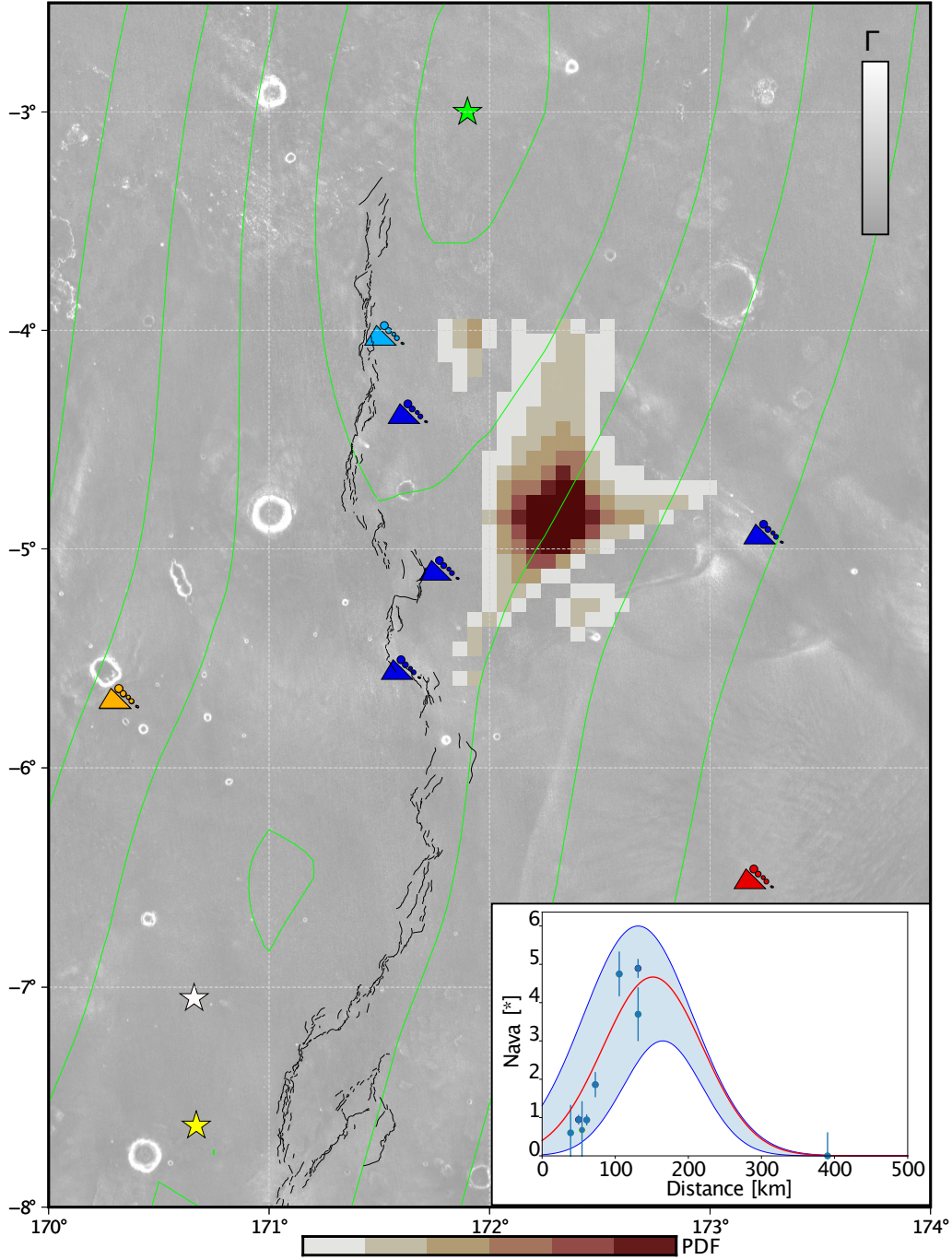


**Figure 5.** Probability distribution of the epicenter inferred from avalanche observations (reddish colormap). Symbols show number of avalanches  $N_{ava}$  due to the S1222a event. The green star (upper center) is the maximum peak of the estimated epicenter and its uncertainty ellipses (green contours) obtained from body waves (Kawamura et al., 2023), the white star, the location estimated from multi-orbit surface waves (Panning et al., 2023), and the yellow star is the estimated epicenter derived from the surface waves (Kim et al., 2022). Black lines are detailed surface traces of the main wrinkle ridge in the vicinity of the epicentral area. Background map is the thermal inertia  $\Gamma$ . (Inset) Expected avalanche density distribution with confidence interval from Monte Carlo inversion using equation 2 with respect to the number of avalanche derived from equation 3.

297 variations in fault strikes are possible along a wrinkle ridge. Note that the wrinkle ridges  
 298 are cross-cutting a large E-W bulge situated at about  $-5^\circ$  latitude, connecting the flanks of  
 299 Apollinaris Patera and a large crater in the west (Fig. 1). This bulge presents hundreds  
 300 of meters of difference in elevation and slight apparent thermal inertia anomalies that  
 301 could indicate a bedrock affected by an old tectonic structure. Interestingly, the bulge's  
 302 azimuth is aligned with our probability distribution of the epicenter. More work would be  
 303 needed to understand the origin of this structure and a possible link with the source of the  
 304 marsquake.

305 It should also be noted that source locations obtained from other methods such as  
 306 surface waves or coda characteristics give different locations (Kim et al., 2022; Panning  
 307 et al., 2023; Menina et al., 2023). Both studies using surface waves predict source loca-  
 308 tions more towards the south as shown in 5. This is due to different back azimuth they  
 309 obtained for surface waves compared from that described in (Kawamura et al., 2023) us-  
 310 ing body waves. Panning et al. (2023) also discusses the possibility that the source loca-  
 311 tion could be in the southern hemisphere. Interestingly, Menina et al. (2023) conclude that  
 312 they need a thick ( 60km) diffusive layer to explain the coda shape of S1222a. This could  
 313 imply that either the source location could be in the highlands of the southern hemisphere  
 314 (Wieczorek et al., 2022), or that thermal anomalies at depth are present in the Appolli-  
 315 naris area.

316 Our work leads us to propose that the source of the quake is likely due to thermal  
 317 contraction due to Mars' cooling through time. The peak of thermal contraction and wrin-  
 318 kle ridge formation occurred during the early Hesperian and decreased progressively until  
 319 now (Watters, 1993). Even if the wrinkle ridge in figure 5 is well expressed in morphol-  
 320 ogy, its surface trace ends to the north, near the transition between Hesperian and Ama-  
 321 zonian terrains (Tanaka et al., 2014). This indicates that the ridge has not been active in  
 322 recent times. However, thermal contraction is still ongoing on Mars and might re-activate  
 323 local mechanical weaknesses in the martian crust, such as wrinkle ridges, over larger re-  
 324 currence time periods. If such activity is real, microseismicity should be associated with  
 325 it.

## 326 4 Conclusions

327 In our comprehensive study of surface features surrounding the S1000a and S1222a  
 328 seismic events on Mars, we utilized MRO orbital data to assess the associated avalanche  
 329 rates. Our findings reveal a substantial increase in avalanches following the S1000a im-  
 330 pact event, suggesting its indirect aftermaths, likely via secondary impacts. The S1222a  
 331 event presented a more complex scenario, necessitating thorough investigation. We estab-  
 332 lished pre-event avalanche rates in line with global estimates from Aharonson et al. (2003)  
 333 and those near Olympus Mons obtained by Heyer et al. (2019), ranging between 1 and  
 334  $6\%.\text{MYear}^{-1}$ . These rates, when compared to post-event rates of up to  $40\%.\text{MYear}^{-1}$   
 335 near the estimated epicenter (Kawamura et al., 2023; Panning et al., 2023; Kim et al.,  
 336 2022), underscore a significant increase in areas of lower apparent thermal inertia. This  
 337 leads us to propose that the S1222a marsquake could be the driving factor behind the ob-  
 338 served increase in avalanches. This analysis also enabled us to estimate a probable epi-  
 339 center for the marsquake, considering the apparent thermal inertia threshold and radial  
 340 ground acceleration. This inferred location is intriguingly situated near a volcanic edi-  
 341 fice and a North-South wrinkle ridge, highlighting the geological complexity of the re-  
 342 gion. Our study not only confirms that current seismic activity on Mars can initiate mass  
 343 wasting processes like dust avalanches but also opens avenues for exploring regions with  
 344 observed avalanches and other seismic events detected by the InSight mission. The in-  
 345 creased rates of avalanches in areas with historical seismic sources suggest that ground  
 346 deformation plays a pivotal role in these phenomena. This methodology can be invaluable  
 347 in future seismic event analyses, where visible aftermaths such as avalanches can offer sig-  
 348 nificant insights into epicenter locations. Overall, our findings demonstrate that avalanches

349 on Mars serve as a crucial tool for documenting rapid processes, from discrete surface  
 350 perturbations like impacts to more continuous events like quakes. This understanding sig-  
 351 nificantly enhances our ability to study and interpret the dynamic surface and subsurface  
 352 processes of Mars

## 353 5 Acknowledgments

354 Author thank Menina S., Margerin L., Kim D., Malystskyy D., Stähler S., Wicz-  
 355 zorek M., Panning M., and Ferrari C. for InSightful discussions. Authors thank Dundas  
 356 C.M. for his help in accessing the post-event HiRISE images for both events. Authors  
 357 thank anonymous reviewers and the associate editor for their constructive feedback. All  
 358 authors declare no conflict of interest. French co-authors acknowledge the French Space  
 359 Agency CNES and ANR (ANR-19-CE31-0008). AL, TK, PL, SR, GS, AM acknowl-  
 360 edge Idex Paris Cité (ANR-18-IDEX-0001). IJD was funded by NASA InSight PSP grant  
 361 80NSSC20K0971.

## 362 6 Open Research

363 The orbital data are available online: HRSC are available at ESA’s Planetary Sci-  
 364 ence Archive (<https://www.cosmos.esa.int/web/psa/mars-express>). THEMIS  
 365 data are available at Arizona State University’s repository (<https://themis.asu.edu>).  
 366 MOC images are available at the PDS Imaging Node ([https://pds-imaging.jpl.nasa.gov/data/mgs-m-moc-na\\_wa-2-sdp-10-v1.0/](https://pds-imaging.jpl.nasa.gov/data/mgs-m-moc-na_wa-2-sdp-10-v1.0/)). MOLA data are available at the  
 367 PDS Geosciences Node (<https://pds-geosciences.wustl.edu/missions/mgs/mola.html>). HiRISE data, including the post-event images, are available at the University  
 368 of Arizona’s dedicated website (<https://www.uahirise.org>). CTX image are available  
 369 at the Imaging PDS Node ([https://pds-imaging.jpl.nasa.gov/data/mro/mars\\_reconnaissance\\_orbiter/ctx/](https://pds-imaging.jpl.nasa.gov/data/mro/mars_reconnaissance_orbiter/ctx/)). The post-event CTX images will be posted on the  
 370 NASA PDS by MSSS by the time of publication. Meanwhile, referee’s can have access to  
 371 the mosaic at <https://www.dropbox.com/sh/u1cykaotwxvi7ga/AAAsDcqw4FrkGDqjb4HTFmjka?dl=0>. The avalanche catalogue is available on Zenodo (doi:10.5281/zenodo.7679315).  
 372 The InSight seismic event catalogue version 9 (InSight Marsquake Service, 2022) and  
 373 waveform data (InSight Mars SEIS Data Service, 2019a,b) are available from the IGP  
 374 Datacenter and IRIS-DMC, as are previous catalogue versions. Seismic waveforms are  
 375 also available from NASA PDS. The crustal thickness grid is available on Zenodo (doi:10.5281/zenodo.6477509).

## 380 References

- 381 Aharonson, O., Schorghofer, N., & Gerstell, M. F. (2003). Slope streak formation and  
 382 dust deposition rates on Mars: Martian slope streak formation rates. *Journal of*  
 383 *Geophysical Research: Planets*, 108(E12). Retrieved 2022-07-14, from <http://doi.wiley.com/10.1029/2003JE002123> doi: 10.1029/2003JE002123  
 384 Andrews-Hanna, J. C. (2020). The tectonic architecture of wrinkle ridges on Mars. *Icarus*,  
 385 351(October 2019), 113937. Retrieved from <https://doi.org/10.1016/j.icarus.2020.113937>  
 386 doi: 10.1016/j.icarus.2020.113937  
 387 Banerdt, W. B., Smrekar, S. E., Banfield, D., Giardini, D., Golombek, M., Johnson, C. L.,  
 388 ... Wiczorek, M. (2020, Mar 01). Initial results from the insight mission on mars.  
 389 *Nature Geoscience*, 13(3), 183-189.  
 390 Baratoux, D., Mangold, N., Forget, F., Cord, A., Pinet, P., Daydou, Y., ... HRSC CO-  
 391 Investigator Team (2006). The role of the wind-transported dust in slope streaks  
 392 activity: Evidence from the HRSC data. *Icarus*, 183(1), 30-45. doi: 10.1016/  
 393 j.icarus.2006.01.023  
 394 Battalio, M., & Wang, H. (2021). The Mars Dust Activity Database (MDAD): A com-  
 395 prehensive statistical study of dust storm sequences. *Icarus*, 354, 114059. Re-

- 397        retrieved 2022-07-14, from [https://linkinghub.elsevier.com/retrieve/pii/](https://linkinghub.elsevier.com/retrieve/pii/S001910352030405X)  
398        S001910352030405X doi: 10.1016/j.icarus.2020.114059
- 399    Bergonio, J. R., Rottas, K. M., & Schorghofer, N. (2013). Properties of martian slope streak  
400        populations. *Icarus*, 225(1), 194-199. Retrieved from [https://www.sciencedirect](https://www.sciencedirect.com/science/article/pii/S0019103513001395)  
401        .com/science/article/pii/S0019103513001395 doi: [https://doi.org/10.1016/](https://doi.org/10.1016/j.icarus.2013.03.023)  
402        j.icarus.2013.03.023
- 403    Bhardwaj, A., Sam, L., Martín-Torres, F. J., Zorzano, M.-P., & Fonseca, R. M. (2017). Mar-  
404        tian slope streaks as plausible indicators of transient water activity. *Scientific Reports*,  
405        7(1), 7074. Retrieved from <https://doi.org/10.1038/s41598-017-07453-9>  
406        doi: 10.1038/s41598-017-07453-9
- 407    Bhardwaj, A., Sam, L., Martín-Torres, F. J., & Zorzano, M.-P. (2019). Are slope streaks  
408        indicative of global-scale aqueous processes on contemporary mars? *Reviews of Geo-*  
409        *physics*, 57(1), 48-77. doi: <https://doi.org/10.1029/2018RG000617>
- 410    Bontemps, N., Lacroix, P., Larose, E., Jara, J., & Taïpe, E. (2020). Rain and small earth-  
411        quakes maintain a slow-moving landslide in a persistent critical state. *Nature Commu-*  
412        *nications*, 11(1), 780.
- 413    Brinkman, N., Stähler, S. C., Giardini, D., Schmelzbach, C., Khan, A., Jacob, A., . . .  
414        Banerdt, W. B. (2021). First focal mechanisms of marsquakes. *Journal of Geo-*  
415        *physical Research: Planets*. Retrieved from [https://agupubs.onlinelibrary](https://agupubs.onlinelibrary.wiley.com/doi/abs/10.1029/2020JE006546)  
416        .wiley.com/doi/abs/10.1029/2020JE006546 doi: [https://doi.org/10.1029/](https://doi.org/10.1029/2020JE006546)  
417        2020JE006546
- 418    Broquet, A., & Andrews-Hanna, J. C. (2022). Geophysical evidence for an active mantle  
419        plume underneath Elysium Planitia on Mars. *Nature Astronomy*. doi: 10.1038/s41550-  
420        022-01836-3
- 421    Brown, J., & Roberts, G. (2019). Possible evidence for variation in magnitude for  
422        marsquakes from fallen boulder populations, Grjota Valles, Mars. *J. Geophys. Res.*  
423        *Planets*, 124(3), 801-812. doi: 10.1029/2018JE005622
- 424    Burleigh, K. J., Melosh, H. J., Tornabene, L. L., Ivanov, B., McEwen, A. S., & Daubar, I. J.  
425        (2012). Impact airblast triggers dust avalanches on mars. *Icarus*, 217(1), 194-201.
- 426    Böse, M., Stähler, S. C., Deichmann, N., Giardini, D., Clinton, J., Lognonné, P., . . . Banerdt,  
427        W. B. (2021, 06). Magnitude Scales for Marsquakes Calibrated from InSight Data.  
428        *Bulletin of the Seismological Society of America*, 111(6), 3003-3015.
- 429    Ceylan, S., Clinton, J. F., Giardini, D., Stähler, S. C., Horleston, A., Kawamura, T., . . .  
430        Banerdt, W. B. (2022). The marsquake catalogue from insight, sols 0–1011. *Physics*  
431        *of the Earth and Planetary Interiors*, 333, 106943.
- 432    Chen, X.-l., Shan, X., Wang, M.-m., Liu, C.-g., & Han, N.-n. (2020, 03). Distribution pat-  
433        tern of coseismic landslides triggered by the 2017 jiuzhaigou ms 7.0 earthquake of  
434        china: Control of seismic landslide susceptibility. *ISPRS International Journal of*  
435        *Geo-Information*, 9, 198. doi: 10.3390/ijgi9040198
- 436    Christensen, P. R., Bandfield, J. L., Hamilton, V. E., Ruff, S. W., Kieffer, H. H., Titus, T. N.,  
437        . . . Greenfield, M. (2001). Mars global surveyor thermal emission spectrometer exper-  
438        iment: Investigation description and surface science results. *Journal of Geophysical*  
439        *Research: Planets*, 106(E10), 23823-23871.
- 440    Christensen, P. R., Jakosky, B. M., Kieffer, H. H., Malin, M. C., Jr, H. Y. M., Nealon, K.,  
441        . . . Ravine, M. (2004). The thermal emission imaging system (themis) for the mars  
442        2001 odyssey mission. In C. T. Russell (Ed.), *2001 mars odyssey* (pp. 85–130). Dor-  
443        drecht: Springer Netherlands.
- 444    Chuang, F. C., Beyer, R. A., McEwen, A. S., & Thomson, B. J. (2007). HiRISE ob-  
445        servations of slope streaks on mars. *Geophysical Research Letters*, 34(20). Re-  
446        trieved from [https://agupubs.onlinelibrary.wiley.com/doi/abs/10.1029/](https://agupubs.onlinelibrary.wiley.com/doi/abs/10.1029/2007GL031111)  
447        2007GL031111 doi: <https://doi.org/10.1029/2007GL031111>
- 448    Clinton, J. F., Ceylan, S., van Driel, M., Giardini, D., Stähler, S. C., Böse, M., . . . Stott, A. E.  
449        (2021). The marsquake catalogue from insight, sols 0–478. *Physics of the Earth and*  
450        *Planetary Interiors*, 310, 106595.
- 451    Davison, A. C., & Hinkley, D. V. (1997). *Bootstrap methods and their application*. Cam-

- bridge University Press.
- 452 Dundas, C. M. (2020). Geomorphological evidence for a dry dust avalanche origin of slope  
453 streaks on mars. *Nature Geoscience*, 13(7), 473–476. Retrieved from [https://doi](https://doi.org/10.1038/s41561-020-0598-x)  
454 [.org/10.1038/s41561-020-0598-x](https://doi.org/10.1038/s41561-020-0598-x) doi: 10.1038/s41561-020-0598-x  
455
- 456 Durand, V., Mangeney, A., Bernard, P., Bonilla, L. F., Satriano, C., Jia, X., . . . Hibert, C.  
457 (Minor revision). The competing role of seismicity and rainfall in slope destabiliza-  
458 tion: rockfalls triggered on a metastable volcanic edifice. *Science Advances*.
- 459 Efron, B., & Tibshirani, R. J. (1993). *An introduction to the bootstrap*. CRC Press.
- 460 Ferguson, R. L., Christensen, P. R., & Kieffer, H. H. (2006, dec). High-resolution ther-  
461 mal inertia derived from the Thermal Emission Imaging System (THEMIS): Ther-  
462 mal model and applications. *Journal of Geophysical Research: Planets*, 111(E12),  
463 n/a–n/a. Retrieved from <http://doi.wiley.com/10.1029/2006JE002735> doi:  
464 10.1029/2006JE002735
- 465 Ferguson, H. M., & Lucchitta, B. K. (1984). *Dark streaks on talus slopes, Mars*. In NASA.  
466 Washington Rept. of Planetary Geol. Programs p 188-190 (SEE N84-23431 13-91).
- 467 Fernando, B., Daubar, I., Grindrod, P., Stott, A., Ateqi, A. A., Atri, D., . . . Banerdt, W.  
468 (2023). Searching for transients or a fresh crater at the origin of insight’s largest  
469 marsquake. *54th Lunar and Planetary Science Conference*, 2806.
- 470 Ferris, J. C., Dohm, J. M., Baker, V. R., & Maddock III, T. (2002). Dark slope streaks on  
471 mars: Are aqueous processes involved? *Geophysical Research Letters*, 29(10), 128-1-  
472 128-4. Retrieved from [https://agupubs.onlinelibrary.wiley.com/doi/abs/](https://agupubs.onlinelibrary.wiley.com/doi/abs/10.1029/2002GL014936)  
473 [10.1029/2002GL014936](https://doi.org/10.1029/2002GL014936) doi: <https://doi.org/10.1029/2002GL014936>
- 474 Gerstell, M. F., Aharonson, O., & Schorghofer, N. (2004). A distinct class of avalanche  
475 scars on Mars. *Icarus*, 168(1), 122–130. Retrieved 2022-07-14, from [https://](https://linkinghub.elsevier.com/retrieve/pii/S0019103503003907)  
476 [linkinghub.elsevier.com/retrieve/pii/S0019103503003907](https://linkinghub.elsevier.com/retrieve/pii/S0019103503003907) doi: 10.1016/  
477 j.icarus.2003.11.005
- 478 Giardini, D., Lognonné, P., Banerdt, W., Pike, W., Christensen, U., Ceylan, S., . . . Yana., C.  
479 (2020). The Seismicity of Mars. *Nature Geoscience*, 13(3), 205–212. doi: [http://](http://doi.org/10.1038/s41561-020-0539-8)  
480 [doi.org/10.1038/s41561-020-0539-8](http://doi.org/10.1038/s41561-020-0539-8)
- 481 Head, J. W., Marchant, D. R., Dickson, J. L., Levy, J. S., & Morgan, G. A. (2007, March).  
482 Slope Streaks in the Antarctic Dry Valleys: Characteristics, Candidate Formation  
483 Mechanisms, and Implications for Slope Streak Formation in the Martian Environ-  
484 ment. In *38th annual lunar and planetary science conference* (p. 1935).
- 485 Heyer, T., Kreslavsky, M., Hiesinger, H., Reiss, D., Bernhardt, H., & Jaumann, R. (2019).  
486 Seasonal formation rates of martian slope streaks. *Icarus*, 323, 76–86. Re-  
487 trieved 2022-07-14, from [https://linkinghub.elsevier.com/retrieve/pii/](https://linkinghub.elsevier.com/retrieve/pii/S0019103518306857)  
488 [S0019103518306857](https://doi.org/10.1016/j.icarus.2019.01.010) doi: 10.1016/j.icarus.2019.01.010
- 489 Heyer, T., Raack, J., Hiesinger, H., & Jaumann, R. (2020). Dust devil triggering of slope  
490 streaks on mars. *Icarus*, 351, 113951. Retrieved from [https://www.sciencedirect](https://www.sciencedirect.com/science/article/pii/S0019103520303249)  
491 [.com/science/article/pii/S0019103520303249](https://doi.org/10.1016/j.icarus.2020.113951) doi: [https://doi.org/10.1016/](https://doi.org/10.1016/j.icarus.2020.113951)  
492 [j.icarus.2020.113951](https://doi.org/10.1016/j.icarus.2020.113951)
- 493 Horvath, D. G., Moitra, P., Hamilton, C. W., Craddock, R. A., & Andrews-Hanna, J. C.  
494 (2021, September). Evidence for geologically recent explosive volcanism in Elysium  
495 Planitia, Mars. *Icarus*, 365, 114499. doi: 10.1016/j.icarus.2021.114499
- 496 InSight Marsquake Service. (2022). *Mars seismic catalogue, insight mission; v12 2022-10-*  
497 *01*. ETHZ, IGP, JPL, ICL, Univ. Bristol. Retrieved from [https://www.insight](https://www.insight.ethz.ch/seismicity/catalog/v12)  
498 [.ethz.ch/seismicity/catalog/v12](https://doi.org/10.12686/a18) doi: 10.12686/a18
- 499 Jacob, A., Plasman, M., Perrin, C., Fuji, N., Lognonné, P., Xu, Z., . . . Banerdt, W. (2022).  
500 Seismic sources of insight marsquakes and seismotectonic context of elysium planitia,  
501 mars. *Tectonophysics*, 837, 229434. Retrieved from [https://www.sciencedirect](https://www.sciencedirect.com/science/article/pii/S0040195122002281)  
502 [.com/science/article/pii/S0040195122002281](https://doi.org/10.1016/j.tecto.2022.229434) doi: [https://doi.org/10.1016/](https://doi.org/10.1016/j.tecto.2022.229434)  
503 [j.tecto.2022.229434](https://doi.org/10.1016/j.tecto.2022.229434)
- 504 Kawamura, T., Clinton, J., Zenhäusern, G., Ceylan, S., Horleston, A., Dahmen, N., . . .  
505 Banerdt, W. (2023). S1222a - the largest Marsquake detected by InSight. *Geophysical*  
506 *Research Letters*. doi: 10.1029/2022GL101543

- 507 Kim, D., Stähler, S. C., Ceylan, S., Lekic, V., Maguire, R., Zenhäusern, G., . . . Banerdt,  
508 W. B. (2022). Structure along the martian dichotomy constrained by rayleigh and  
509 love waves and their overtones. *Geophysical Research Letters*, e2022GL101666.
- 510 Knapmeyer, M., Oberst, J., Hauber, E., Wählisch, M., Deuchler, C., & Wagner, R. (2006).  
511 Working models for spatial distribution and level of Mars' seismicity. *J. Geophys. Res.*  
512 *E Planets*, 111(11), 1–23. doi: 10.1029/2006JE002708
- 513 Knapmeyer, M., Stähler, S., Plesa, A.-C., Ceylan, S., Charalambous, C., Clinton, J., . . .  
514 Banerdt, W. B. (2023). The global seismic moment rate of mars after event s1222a.  
515 *Geophysical Research Letters*, 50(7), e2022GL102296.
- 516 Kreslavsky, M. A., & Head, J. W. (2009). Slope streaks on Mars: A new "wet" mecha-  
517 nism. *Icarus*, 201(2), 517–527. Retrieved 2022-07-14, from [https://linkinghub](https://linkinghub.elsevier.com/retrieve/pii/S0019103509000608)  
518 [.elsevier.com/retrieve/pii/S0019103509000608](https://linkinghub.elsevier.com/retrieve/pii/S0019103509000608) doi: 10.1016/j.icarus.2009  
519 .01.026
- 520 Livio, F., & Ferrario, M. F. (2020). Assessment of attenuation regressions for earthquake-  
521 triggered landslides in the italian apennines: insights from recent and historical events.  
522 *Landslides*, 17(12), 2825–2836.
- 523 Lognonné, P., Banerdt, W. B., Giardini, D., Pike, W. T., Christensen, U., Laudet, P., . . .  
524 Wookey, J. (2019, feb). SEIS: Insight's Seismic Experiment for Internal Structure  
525 of Mars. *Space Science Reviews*, 215(1), 12. Retrieved from [http://dx.doi.org/](http://dx.doi.org/10.1007/s11214-018-0574-6)  
526 [10.1007/s11214-018-0574-6](http://dx.doi.org/10.1007/s11214-018-0574-6)<http://link.springer.com/10.1007/s11214>  
527 [-018-0574-6](http://link.springer.com/10.1007/s11214-018-0574-6) doi: 10.1007/s11214-018-0574-6
- 528 Lombardo, L., & Tanyas, H. (2022). From scenario-based seismic hazard to scenario-based  
529 landslide hazard: fast-forwarding to the future via statistical simulations. *Stoch Envi-*  
530 *ron Res Risk Assess*, 36, 2229–2242.
- 531 Lucas, A. (2010). *Dynamique des instabilités gravitaires par modélisation et télédétection:*  
532 *Applications aux exemples martiens* (Theses, Institut de physique du globe de paris -  
533 IPGP). Retrieved from <https://tel.archives-ouvertes.fr/tel-00503212>
- 534 Lucas, A., & Mangeney, A. (2007). Mobility and topographic effects for large valles  
535 marineris landslides on mars. *Geophysical Research Letters*, 34(10).
- 536 Lucas, A., Mangeney, A., & Ampuero, J. P. (2014). Frictional velocity-weakening in land-  
537 slides on earth and on other planetary bodies. *Nature Communications*, 5(1), 3417.
- 538 Lucas, A., Mangeney, A., Mège, D., & Bouchut, F. (2011). Influence of the scar geometry  
539 on landslide dynamics and deposits: Application to martian landslides. *Journal of*  
540 *Geophysical Research: Planets*, 116(E10).
- 541 Maguire, R. R., Lekić, V., Schmerr, N. C., Kim, D., Li, J., Beghein, C., . . . Bruce Banerdt,  
542 W. (2023). Moment Tensor Estimation of Event S1222a and Implications for Tec-  
543 tonics Near the Dichotomy Boundary in Southern Elysium Planitia Mars. *Journal of*  
544 *Geophysical Research E: Planets*, submitted.
- 545 Malin, M. C., Bell, J. F., Cantor, B. A., Caplinger, M. A., Calvin, W. M., Clancy, R. T., . . .  
546 Wolff, M. J. (2007, may). Context Camera Investigation on board the Mars Reconnaissance  
547 Orbiter. *Journal of Geophysical Research*, 112(E5), E05S04. Retrieved from  
548 <http://doi.wiley.com/10.1029/2006JE002808> doi: 10.1029/2006JE002808
- 549 Martino, S., Fiorucci, M., Marmoni, G. M., Casaburi, L., Antonielli, B., & Mazzanti, P.  
550 (2022). Increase in landslide activity after a low-magnitude earthquake as inferred  
551 from dinsar interferometry. *Scientific Reports*, 12(1), 2686.
- 552 McEwen, A. S., Eliason, E. M., Bergstrom, J. W., Bridges, N. T., Hansen, C. J., Delamere,  
553 W. A., . . . Weitz, C. M. (2007, may). Mars Reconnaissance Orbiter's High Resolution  
554 Imaging Science Experiment (HiRISE). *Journal of Geophysical Research*, 112(E5),  
555 E05S02. Retrieved from <http://doi.wiley.com/10.1029/2005JE002605> doi:  
556 10.1029/2005JE002605
- 557 Menina, S., Margerin, L., Kawamura, T., Heller, G., Drilleau, M., Xu, Z., . . . Banerdt, W. B.  
558 (2023). Stratification of heterogeneity in the lithosphere of mars from envelope mod-  
559 eling of event s1222a and near impacts: Interpretation and implications for very-high-  
560 frequency events. *Geophysical Research Letters*, 50(7), e2023GL103202.
- 561 Miyamoto, H. (2004). Fluid dynamical implications of anastomosing slope streaks on Mars.

- 562 *Journal of Geophysical Research*, 109(E6), E06008. Retrieved 2022-07-14, from  
 563 <http://doi.wiley.com/10.1029/2003JE002234> doi: 10.1029/2003JE002234
- 564 Mosegaard, K., & Tarantola, A. (1995). Monte carlo sampling of solutions to inverse prob-  
 565 lems. *Journal of Geophysical Research: Solid Earth*, 100(B7), 12431-12447. doi:  
 566 <https://doi.org/10.1029/94JB03097>
- 567 Neukum, G., & Jaumann, R. (2004). The high resolution stereo camera of mars express. *ESA*  
 568 *Special Publication*, 1240, 1–19.
- 569 Panning, M. P., Banerdt, W. B., Beghein, C., Carrasco, S., Ceylan, S., Clinton, J. F., . . . Zen-  
 570 häusern, G. (2023). Locating the largest event observed on mars with multi-orbit  
 571 surface waves. *Geophysical Research Letters*, 50(1), e2022GL101270.
- 572 Perrin, C., Jacob, A., Lucas, A., Myhill, R., Hauber, E., Batov, A., . . . Fuji, N. (2022). Ge-  
 573 ometry and segmentation of cerberus fossae, mars: Implications for marsquake proper-  
 574 ties. *J. Geophys. Res.: Planets*, 127(1), e2021JE007118. doi: [https://doi.org/10.1029/](https://doi.org/10.1029/2021JE007118)  
 575 [2021JE007118](https://doi.org/10.1029/2021JE007118)
- 576 Phillips, C. B., Burr, D. M., & Beyer, R. A. (2007). Mass movement within a slope streak  
 577 on mars. *Geophysical Research Letters*, 34(21). Retrieved from [https://agupubs](https://agupubs.onlinelibrary.wiley.com/doi/abs/10.1029/2007GL031577)  
 578 [.onlinelibrary.wiley.com/doi/abs/10.1029/2007GL031577](https://doi.org/10.1029/2007GL031577) doi: [https://](https://doi.org/10.1029/2007GL031577)  
 579 [doi.org/10.1029/2007GL031577](https://doi.org/10.1029/2007GL031577)
- 580 Posiolova, L. V., Lognonné, P., Banerdt, W. B., Clinton, J., Collins, G. S., Kawamura, T., . . .  
 581 Zenhäusern, G. (2022). Largest recent impact craters on mars: Orbital imaging and  
 582 surface seismic co-investigation. *Science*, 378(6618), 412-417.
- 583 Roberts, G. P., Matthews, B., Bristow, C., Guerrieri, L., & Vetterlein, J. (2012, February).  
 584 Possible evidence of paleomarsquakes from fallen boulder populations, Cerberus Fos-  
 585 sae, Mars. *J. Geophys. Res. Planets*, 117(E2), n/a-n/a. doi: 10.1029/2011JE003816
- 586 Rosser, N., Kinsey, M., Oven, K., Densmore, A., Robinson, T., Pujara, D. S., . . . Dhital,  
 587 M. R. (2021). Changing significance of landslide hazard and risk after the 2015 mw  
 588 7.8 gorkha, nepal earthquake. *Progress in Disaster Science*, 10, 100159.
- 589 Schorghofer, N., Aharonson, O., Gerstell, M., & Tatsumi, L. (2007). Three decades of  
 590 slope streak activity on mars. *Icarus*, 191(1), 132-140. Retrieved from [https://](https://www.sciencedirect.com/science/article/pii/S0019103507001960)  
 591 [www.sciencedirect.com/science/article/pii/S0019103507001960](https://www.sciencedirect.com/science/article/pii/S0019103507001960) doi:  
 592 <https://doi.org/10.1016/j.icarus.2007.04.026>
- 593 Schorghofer, N., Aharonson, O., & Khatiwala, S. (2002). Slope streaks on Mars: Correla-  
 594 tions with surface properties and the potential role of water: Slope streaks on Mars.  
 595 *Geophysical Research Letters*, 29(23), 41–1–41–4. Retrieved 2022-07-14, from  
 596 <http://doi.wiley.com/10.1029/2002GL015889> doi: 10.1029/2002GL015889
- 597 Schorghofer, N., & King, C. M. (2011). Sporadic formation of slope streaks on Mars. *Icarus*,  
 598 216(1), 159–168. Retrieved 2022-07-14, from [https://linkinghub.elsevier](https://linkinghub.elsevier.com/retrieve/pii/S0019103511003459)  
 599 [.com/retrieve/pii/S0019103511003459](https://doi.org/10.1016/j.icarus.2011.08.028) doi: 10.1016/j.icarus.2011.08.028
- 600 Smith, D. E., Zuber, M. T., Frey, H. V., Garvin, J. B., Head, J. W., Muhleman, D. O., . . .  
 601 Sun, X. (2001). Mars orbiter laser altimeter: Experiment summary after the first  
 602 year of global mapping of mars. *Journal of Geophysical Research: Planets*, 106(E10),  
 603 23689-23722.
- 604 Stähler, S. C., Mittelholz, A., Perrin, C., Kawamura, T., Kim, D., Knapmeyer, M., . . .  
 605 Banerdt, W. B. (2022). Tectonics of Cerberus Fossae unveiled by marsquakes. *Nature*  
 606 *Astronomy*, 6(12), 1376–1386. doi: 10.1038/s41550-022-01803-y
- 607 Sullivan, R., Thomas, P., Veverka, J., Malin, M., & Edgett, K. S. (2001). Mass movement  
 608 slope streaks imaged by the mars orbiter camera. *Journal of Geophysical Research:*  
 609 *Planets*, 106(E10), 23607-23633. doi: <https://doi.org/10.1029/2000JE001296>
- 610 Tanaka, K., Skinner, J., Jr., D., J.M., I., Irwin R.P., Kolb, E., Fortezzo, C., . . . Hare, T.  
 611 (2014). Geologic map of mars. *U.S. Geological Survey Scientific, pamphlet 43 p.*  
 612 doi: 10.3133/sim3292
- 613 Tatard, L. (2010). *Statistical analysis of triggered landslides : implications for earthquake*  
 614 *and weather controls* (Unpublished doctoral dissertation). University of Canterbury  
 615 and Université de Grenoble.
- 616 Valantinas, A., Becerra, P., Pommerol, A., Tornabene, L., Affolter, L., Cremonese, G., . . .

- 617 Thomas, N. (2021). CaSSIS color and multi-angular observations of Martian slope  
618 streaks. *Planetary and Space Science*, 209, 105373. Retrieved 2022-07-14, from  
619 <https://linkinghub.elsevier.com/retrieve/pii/S0032063321002129> doi:  
620 10.1016/j.pss.2021.105373
- 621 Watters, T. R. (1993). Compressional tectonism on Mars. *Journal of Geophysical Research*,  
622 98(E9), 17049. Retrieved from <http://doi.wiley.com/10.1029/93JE01138> doi:  
623 10.1029/93JE01138
- 624 Wieczorek, M. A., Broquet, A., McLennan, S. M., Rivoldini, A., Golombek, M., Antonan-  
625 geli, D., . . . Banerdt, W. B. (2022). Insight constraints on the global character of the  
626 martian crust. *Journal of Geophysical Research: Planets*, 127(5), e2022JE007298.